ChemPhotoChem

ChemPhotoChem

Chemistry Europe
European Chemical Societies Publishing

REVIEW OPEN ACCESS

Cationic Doping Strategies in Metal Oxide Photocatalysts for Solar Water Splitting

Mengqi Duan | Yiyang Li | Shik Chi Edman Tsang[†]

Department of Chemistry, University of Oxford, Oxford, U.K.

Correspondence: Yiyang Li (yiyang.li@chem.ox.ac.uk)

Received: 30 October 2025 | **Revised:** 12 March 2026 | **Accepted:** 13 March 2026

Keywords: cation doping | photocatalysis |semiconductor

ABSTRACT

Photocatalytic water splitting is a promising method for green hydrogen production. Great progress has been made in photocatalyst activity after decades of study. Cationic doping is one of the most extensively studied photocatalyst optimization strategies. Diverse findings, both positive and negative effects, have been reported, reflecting the complexity of the system. Thus, a deep understanding of both the fundamentals and current progress is essential for the rational exploration and development of this strategy. In this *Review*, we start by providing a brief introduction to the principles of photocatalytic water splitting and the evaluation indices of photocatalytic efficiency. Following that, we present the fundamentals of cationic doping, with special attention to the underlying thermodynamics and its modification of the structure and electronic structure of metal oxide photocatalysts. Building on this basis, we highlight recent progress in understanding how cationic doping affects fundamental steps in photocatalytic water splitting, with a focus on light absorption and charge transport. Finally, we summarize the current challenges and research gaps in the field.

1 | Introduction

Hydrogen (H_2) has broad applications in multiple sectors, including transportation, chemical manufacturing, power generation, and energy storage, and thus producing green hydrogen from renewable energy plays an important role in energy conservation, emission reduction, and sustainable development [1] [2]. Photocatalytic water splitting, catalyzed by semiconductor photocatalysts, which directly converts solar energy into hydrogen, has attracted tremendous research interest due to its potential for scalability, simplicity, and low cost in production facilities and operation [3] [4] [5]. Great advances in photocatalyst performance have been made since the pioneering work on semiconductor reactivity in electrolytes under illumination conditions by Gerischer in 1966 [6] and the milestone report of photocatalytic water splitting on TiO_2 by Fujishima and Honda in 1972 [7].

Metal oxides constitute a dominant class of photocatalysts for water splitting due to their thermodynamically satisfactory band structures, low cost, and stability. However, the large band gap and rapid charge carrier recombination lead to low catalytic activity. A wide range of strategies has been studied to improve their performance, including doping [8], constructing heterostructures [9], loading cocatalysts [10], introducing functional groups on the surface [11], and applying external electric/magnetic fields [12]. Among these, doping has been economically viable and particularly effective in tuning photocatalytic activity by altering the structural and electronic properties of photocatalysts [13–15].

Crucially, cationic doping has shown a complex influence on photocatalysis across diverse reports. Some studies report notable gains in activity. For example, Domen et al. developed an $SrTiO_3$-based photocatalyst platform that achieved quantum efficiencies approaching unity through substitutional Al doping [14]. Others report negligible or detrimental effects on the overall

---

[†] Deceased on May 20, 2025.

photocatalytic activity, despite enhancements in certain properties, such as extended light absorption or prolonged photogenerated charge carrier lifetime [16]. For example, Kudo et al. reported that although light absorption was extended, Rh doping suppressed the activity of TiO_2 for the photocatalytic oxygen evolution reaction because of the increased recombination of photogenerated charge carriers at Rh^{4+} states [17]. These contrasting results underscore the complexity of engineering metal oxide photocatalysts with cationic doping.

To understand the complexities and guide rational design, it is helpful to conduct a systematic review of underlying principles and recent progress. In this review, we discuss the effect of cationic doping on the structure and function of metal oxide photocatalysts for water splitting within the framework of metal oxide photocatalyst systems, with a primary focus on several representative photocatalysts, such as TiO_2, $SrTiO_3$, and exfoliated layered perovskite $TBACa_2Nb_3O_{10}$. We start by outlining the key steps in photocatalytic water splitting and photocatalyst performance evaluation indices. Next, we review the thermodynamics underlying cationic doping and the induced modifications in the structure and electronic structure of the metal oxide photocatalysts. Then we highlight recent progress on the influence of cationic doping on fundamental catalytic steps (light absorption, charge transport, and surface reactions). Finally, we discuss the current challenges and gaps in this field.

2 | Photocatalytic Water Splitting on Metal Oxides

2.1 | Fundamental Steps

Generally, three sequential steps are involved in photocatalytic water splitting on a semiconductor (Figure 1a,b): (I) absorption of light and generation of excitons (femtosecond timescale): a semiconductor photocatalyst absorbs photons with energy greater than its bandgap energy, exciting valence band electrons to conduction band and creating valence band holes and conduction band electrons; (II) separation and migration of charge carriers (nanosecond to microsecond timescale): some of the electrons and holes get separated, become free carriers and migrate to active sites on the surface, while others recombine either immediately after excitation or along their migration to the surface, generating heat or fluorescence; (III) surface reaction (millisecond to second timescale): H_2O adsorbed on the catalyst surface gets reduced at electron sites and oxidized at hole sites, forming H_2 and O_2 separately [2, 18]. Typically, cocatalysts for hydrogen evolution reaction (HER) and OER would be loaded on semiconductors as the reaction sites to promote fast reaction kinetics and suppress backward reactions.

2.2 | Thermodynamics

To drive overall water splitting and achieve stoichiometric evolution of H_2 and O_2, the electrochemical potential of photogenerated electrons and holes should be sufficient to provide thermodynamic driving force and overcome mass-transport and kinetic energy losses during the migration and catalytic reaction. Importantly, the electrochemical potential of photogenerated charge carriers is sensitive to the local environment, surface chemistry, and charge transfer kinetics [19]. Recent studies revealed that the local chemical environment under experimental conditions and surface terminal groups modulate the surface energetics [20, 21]. Under operating conditions, differences in the kinetics of electron and hole transfer can lead to depletion, accumulation, or inversion of excess charge carriers (Figure 2a–c). The resulting internal electric field shifts the electrochemical potential of charge carriers and the band edges, thereby increasing the reducing or oxidizing power of photoexcited electrons or holes. Additionally, evolved gas can also alter the surface energetics. For example, H_2 and O_2 adsorbed at Pt/p-Si catalyst surface induce interfacial dipoles, which tune the charge carrier selectivity by modulating the Schottky barrier height, and the in-situ generated SiO_x interlayer suppresses recombination by facilitating tunneling-mediated charge transfer (Figure 2d–f) [20]. Furthermore, spatially inhomogeneous kinetics of charge carrier transfer lead to spatially varying energetics across the interface, which sensitively

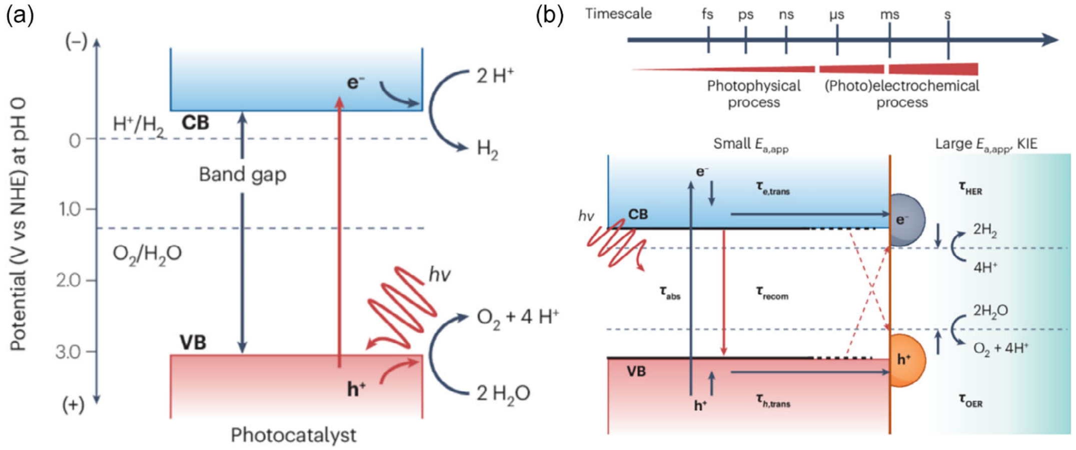

FIGURE 1 | Fundamental steps for photocatalytic water splitting. (a) Photocatalytic water splitting fundamental steps. (b) Time scale of the fundamental steps. τ_{abs}, timescale for absorption; $\tau_{e,\ trans}$, timescale for electron transfer; τ_{HER}, timescale for HER; $\tau_{h,\ trans}$, timescale for hole transfer; τ_{OER}, timescale for OER; τ_{recom}, timescale for recombination; VB, valence band; CB, conduction band; $E_{a,\ app}$, apparent activation energy; HER, hydrogen evolution reaction; KIE, kinetic isotope effect; NHE, normal hydrogen electrode; OER, oxygen evolution reaction. Figure 1a,b reprinted with permission from Ref. [1], copyright (2025) Springer Nature Limited.

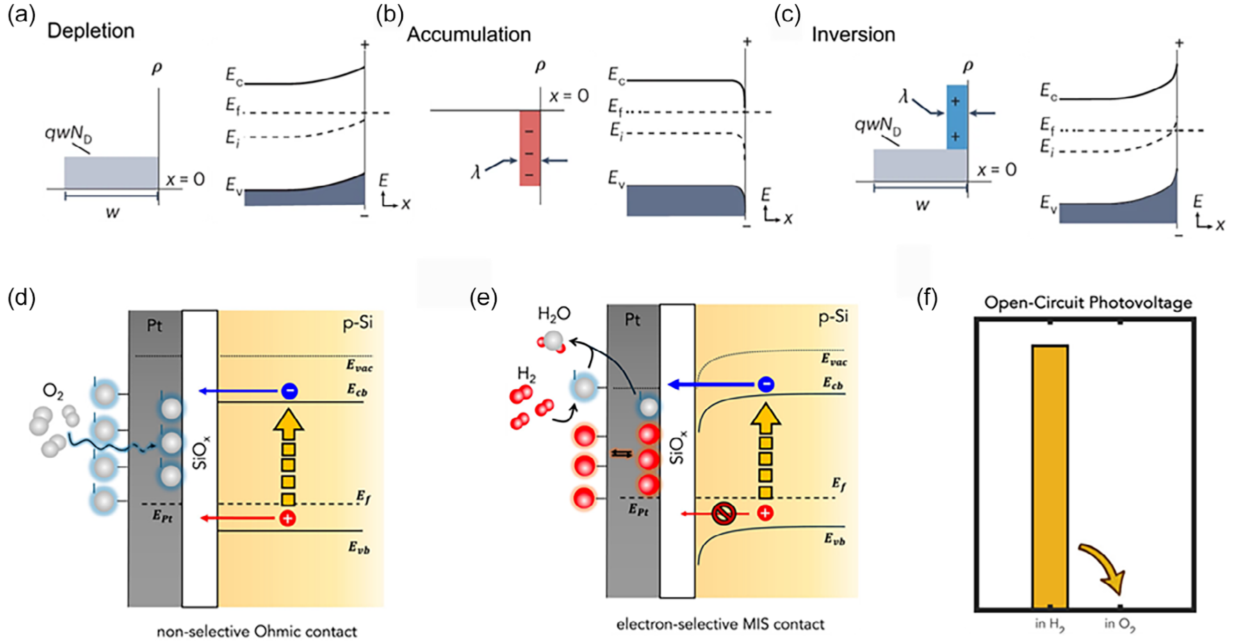

FIGURE 2 | Dynamic surface energetics. Excess charge-carrier-density plots and corresponding band diagrams for an n-type semiconductor in (a) depletion, (b) accumulation, and (c) inversion due to equilibration with a contacting phase, such as redox species. Mechanisms for dipole-mediated barrier formation: (d) O_2 adsorption and diffusion lead to O_{ad} on the Pt surface and the Pt/SiO_x interface with partial electronegative charge, increasing the effective work function and leading to nonselective Ohmic behavior. (e) H_2 spontaneously reacts with O_{ad} to form water, cleans the surface and the interface, and neutralizes the negative dipole. As a result, the effective work function decreases, leading to band bending with substantial barriers and electron selectivity. E_{vac}, vacuum energy; E_{cb}, conduction band edge; E_{vb}, valence band edge; $E_{f,\ s}$, Fermi level of p-Si; $E_{f,\ Pt}$, Fermi level of Pt. (f) Comparison of open-circuit photovoltage in H_2 and O_2. Figure 2a-c adapted with permission from Ref. [19], copyright (2024) Springer Nature Limited. Figure 2d-f reprinted with permission from Ref. [20], copyright (2025) American Chemical Society.

affects charge-separation efficiency [21]. These findings address the dynamic nature of the driving force for photocatalytic water splitting and suggest that the commonly used absolute band edge potential diagrams or tables for the identification of appropriate photocatalysts, where the valence band maximum should be more positive than 1.23 V vs NHE and the conduction band minimum should be more negative than 0 V vs NHE (pH = 0), should be used and interpreted with caution.

For a comprehensive understanding of photocatalytic water splitting, we refer readers to the work of Domen et al. and the review by Boettcher et al. for thermodynamics and kinetics [2, 19], the work of Cortes et al. for charge transport [22], and the work of Tsang et al. for surface reaction mechanism [23].

2.3 | Efficiency Evaluation

The overall photocatalytic water splitting efficiency depends on the efficiency of each fundamental step mentioned above [22]. Therefore, the overall solar energy conversion efficiency is a product of efficiencies of the three fundamental steps, as described below:

$$\eta_{total} = \eta_{absorption} \times \eta_{separation} \times \eta_{reaction} \qquad (1)$$

where $\eta_{absorption}$ refers to the photon absorption efficiency, defined as the ratio of photogenerated electron–hole pairs to incident photons. $\eta_{separation}$ refers to the separation efficiency, defined as the fraction of photogenerated charge carriers that separate and migrate to the surface of the photocatalysts. $\eta_{reaction}$ refers to the surface catalysis reaction efficiency.

When evaluating photocatalyst efficiency, three reaction systems are typically considered (Figure 3a–c) [3, 24]:

(I) One-step excitation overall water splitting without sacrificial reagents. In this system, HER and OER occur on the same photocatalyst system. A single photocatalyst has suitable band energetics and can drive the overall water splitting.

(II) Sacrificial reagent-assisted half-reactions: The system employs a hole scavenger or an electron acceptor to make the reaction thermodynamically easier. For HER activity evaluation, a hole scavenger such as methanol is used. Photogenerated holes in the valence band irreversibly oxidize methanol, while photogenerated electrons in the conduction band reduce water to produce H_2. For OER activity evaluation, an electron acceptor such as $AgNO_3$ is employed. Photogenerated electrons in the conduction band irreversibly reduce Ag^+, and photogenerated holes in the valence band oxidize H_2O to produce O_2. This system is useful for evaluating photocatalyst performance in half reactions rather than overall water-splitting capability.

(III) Two-step excitation (Z-scheme) overall water splitting: The system is an attempt to mimic Photosystem I and Photosystem II processes in green plants. It typically includes an HER photocatalyst and an OER photocatalyst together with a shuttle redox mediator. On HER photocatalyst, photogenerated electrons in conduction band reduce H_2O to form H_2, and the photogenerated holes oxidize mediators. Simultaneously, on the OER photocatalyst, photogenerated holes in the valence band oxidize H_2O to

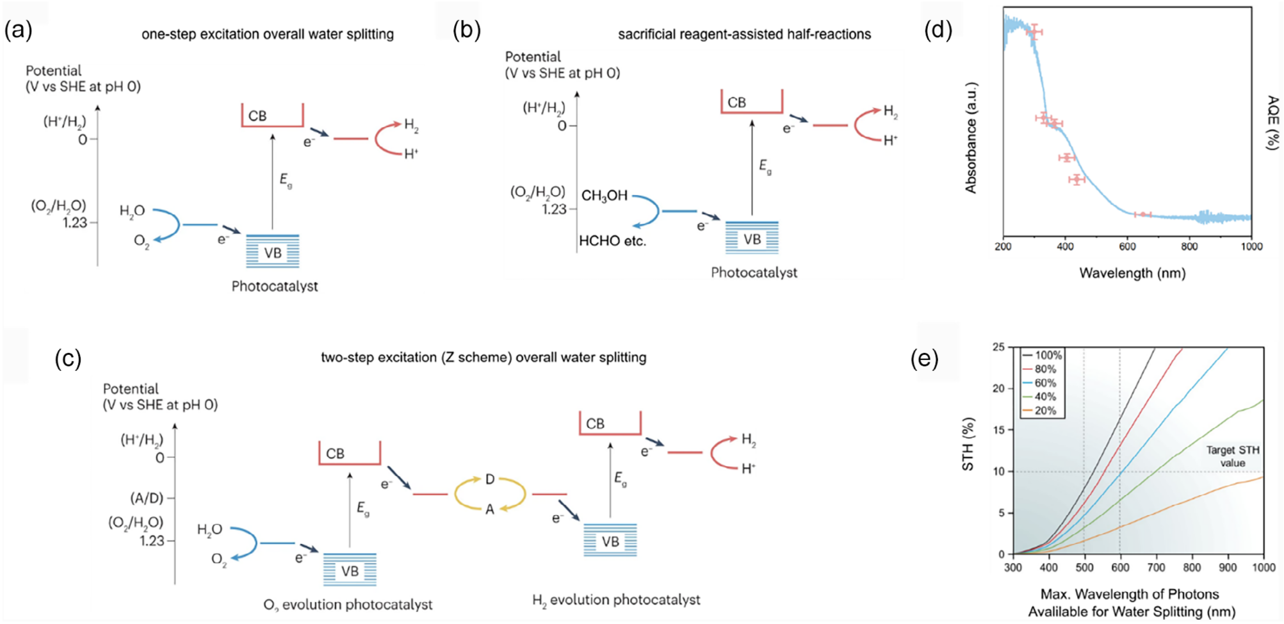

FIGURE 3 | Photocatalytic reaction system and photocatalytic activity evaluation indexes. (a) One-step excitation overall water splitting with single absorber. (b) Sacrificial reagent-assisted half reaction in water splitting. In this case, methanol is used as sacrificial reagent. Photogenerated holes oxidize methanol to formaldehyde, while photogenerated electrons reduce H_2O to H_2. (c) Two-step excitation (Z-scheme) overall water splitting using dual-absorber photocatalysts. A, electron-accepting species; CB, conduction band; D, electron-donating species; E_g, bandgap energy of a semiconductor; SHE, standard hydrogen electrode; VB, valence band. (d) The apparent quantum efficiency (AQE) decreases progressively with increasing wavelength. (e) Relationship between the STH and photon wavelength at different AQEs. Figure 3a–c adapted with permission from Ref. [4], copyright (2023) Springer Nature Limited. Figure 3d reproduced under terms of the CC-BY license [13]. Copyright (2025), The Authors, published by the American Chemical Society. Figure 3e adapted with permission from Ref. [18], copyright (2017) Springer Nature Limited.

form O_2, while the photogenerated electrons in the conduction band reduce mediators. During the process, mediators can be regenerated, and overall water splitting can be achieved. This system relaxes the band-energetic requirements for a single photocatalyst because it couples two photocatalysts, each of which only needs to satisfy the requirement for half reactions. The factors that affect one-step excitation water splitting by a single photocatalyst are also applicable to this system. In some cases where the shuttle redox mediators are absent, an interparticle physical contact or a solid-state electron conductor can be employed to transfer charge carriers between HER and OER photocatalysts.

Photocatalyst performance is usually evaluated by the following indices:

(I) H_2 evolution rate: it indicates how fast H_2 is produced in a photocatalytic system under a given catalyst loading and is usually reported in the unit of μmol h^{-1}.

(II) Photocatalytic activity: it reflects the reaction rate per unit mass of photocatalyst, representing the intrinsic catalytic ability, which is a critical parameter for catalyst design and scale-up. Reporting both the absolute values of the hydrogen evolution rate and the mass-normalized values provides a balanced view of catalytic performance.

(III) Apparent quantum efficiency (AQE): As it is not practical to directly measure photons absorbed by heterogeneous photocatalysts because of light scattering by catalyst particles, the incident photons are generally measured to calculate AQE. It is the ratio of the number of H_2 molecules evolved to the number of incident photons of a specific energy and reflects the photocatalyst performance at different wavelengths, and is defined as follows:

$$\text{AQE}\,(\%) = \frac{2\times\text{Number of H}_2}{\text{Number of incident photons}}\times 100\% \qquad (2)$$

AQE generally decays with the increase in wavelength, indicating a large proportion of charge carriers excited by lower energy photons are inactive in the catalytic reaction (Figure 3d). Several factors affect this. First, the photoexcited charge carriers located at defective levels might lack the necessary driving force to satisfy the thermodynamic requirements for water splitting. Second, the charge carriers generated at longer wavelengths tend to have lower kinetic energy, which might not allow the charge carriers to overcome energy losses in mass transport and the catalytic reaction. Third, the generation of polarons can render charge carriers inactive due to decreased activity of ligand field transitions that dominate in the visible light range [25]. Thus, extended light absorption alone cannot account for dramatically enhanced photocatalytic activity. Instead, their effects on charge transport and surface reactions play a more dominant role in the enhancement of activity.

(IV) Solar-to-hydrogen conversion efficiency (STH): It is defined as the ratio of chemical energy that can be released by combustion of evolved H_2 to the solar energy input during photocatalysis, which indicates the overall energy conversion efficiency of photocatalysts, and is described as follows:

$$\text{STH}\,(\%) = \frac{\Delta G\times\text{Number of H}_2}{P\times S\times T}\times 100\% \qquad (3)$$

where P is the solar irradiance (0.1 W cm^{-2}), S is the illuminated area given in $cm^{-2,}$ T is the reaction time in seconds, ΔG is the Gibbs free energy for the photocatalytic water splitting reaction under the reaction conditions, and the number of H_2 is given in moles. STH can only be used in the overall water splitting reaction system. The relationship between STH and the wavelengths of photons available in AM 1.5 at different AQEs for photocatalytic water splitting indicates the importance of developing photocatalysts with narrow band gaps (Figure 3e).

To accurately evaluate activity and avoid overestimation or underestimation of AQE and STH, several factors in the reaction system must be controlled carefully. Firstly, the reaction system should be completely degassed by vacuum or a flow of inert gas before catalytic reactions to ensure the measured gases evolve from the reaction instead of air. Besides, the water quality should be carefully controlled to prevent the influence of inorganic ions and organic impurities. Furthermore, gas chromatographs must be carefully calibrated using standard gases for accurate quantification of evolved gases. Careful control of temperature during the reaction is also necessary, as temperature affects the reaction kinetics and pathways. Additionally, photocatalyst mass should be optimized. At low loading, gas production generally increases with catalyst amount, but excessive loading causes stronger light scattering and shielding, which lowers apparent activity. In that case, the measured activity no longer reflects intrinsic catalyst performance. Moreover, the averaging period used to calculate reaction rates should be reported because initial activity often differs from long-term activity due to activation or deactivation. Besides, the light intensity, wavelength, and irradiance area should be carefully controlled and evaluated. For a detailed overview of catalyst performance testing and evaluation practices, we recommend the primer by Maeda et al. [4]

3 | Thermodynamics Underlying Cationic Doping

The incorporation of cationic dopants is governed by intrinsic factors such as the composition and phase of metal oxide hosts and dopant size and charge mismatch with host cations, and external parameters such as temperature and pressure [26]. These factors determine the thermodynamics of dopant incorporation and doping limitations. In this section, we briefly outline the thermodynamic principles underlying doping and summarize the classification of materials based on their dopability as revealed by defect diagrams derived from first-principles calculations.

For successful spontaneous cationic doping, the change in Gibbs free energy must be negative, i.e.,

$$\Delta G = \Delta H - T\Delta S < 0 \tag{4}$$

where ΔH denotes the enthalpy of cationic dopant formation, ΔS refers to the change in entropy, which is a sum of vibrational entropy (ΔS_{vib}), thermal entropy ($\Delta S_{\mathrm{thermal}}$), and configurational entropy ($\Delta S_{\mathrm{config}}$), and T is the absolute temperature.

In the case of substitutional cationic doping with a site fraction of X_c, the enthalpy is given by:

$$\Delta H \approx X_c \Delta H_c \tag{5}$$

The nonconfigurational entropy, including vibrational entropy and thermal entropy, is given by:

$$\Delta S_{\mathrm{nonconfig}} \approx X_c \Delta S_{\mathrm{vib}} \tag{6}$$

The configurational entropy is given by:

$$\Delta S_{\mathrm{config}} = -R[X ln X_c + (1 - X_c)\ln(1 - X_c)] \tag{7}$$

Therefore, the change in Gibbs free energy can be expressed as a function of the site fraction of the cationic dopant:

$$\Delta G_c \approx X_c \Delta H_c - T X_c \Delta \mathrm{H}_c + RT[X \ln X_c + (1 - X_c)\ln(1 - X_c)] \tag{8}$$

At equilibrium, the Gibbs free energy is at the minimum. By solving the first derivation of the equation and assuming the equilibrium cationic dopant fraction $X_c^e \ll 1$, we obtain X_c^e is related to temperature, ΔH_c, and ΔS_{vib}:

$$X_c^e = \exp\left(\frac{\Delta S_{\mathrm{vib}}}{R}\right) \exp\left(-\frac{\Delta H_c}{\mathrm{RT}}\right) \tag{9}$$

where ΔH_c and ΔS_{vib} are sensitive to intrinsic properties, such as intrinsic defects, the composition and phases of metal oxides, dopant size and charge mismatch with host cations, and to external parameters such as temperature and pressure. Therefore, when adopting cationic doping strategies to modify photocatalysts, these internal and external thermodynamic factors should be carefully considered and controlled. Take $SrTiO_3$ as an example. As an internal factor, the dopant size mismatch with host can cause dramatic differences in solubility. Both La^{3+} and Eu^{3+} can substitute Sr^{2+}. However, the solubility of La^{3+} and Eu^{3+} in $SrTiO_3$ has a large difference. Because La^{3+} (1.36 Å, CN = 12) has a relatively small ionic radius mismatch with Sr^{2+} (1.44 Å, CN = 12) the enthalpy and entropy of substitution are relatively small. As a result, the solubility of La^{3+} can be up to 40 at% [27]. In contrast, Eu^{3+} (1.01 Å, CN = 12) has a larger size mismatch with Sr^{2+}, enthalpy of substitution dramatically increases, leading to a significantly lower solubility of only 1–2 at% [28]. In addition, external factors also impose a significant effect. For example, oxygen partial pressure can affect the doping limits of La. At a fixed temperature of 850°C, the La doping amount was increased with the decrease in oxygen partial pressure from 1×10^{-1} to 1×10^{-8} Torr by shifting defect equilibria [29].

Since these thermodynamic quantities can be analyzed with first-principles calculations, the ease of incorporating extrinsic dopants, termed dopability, can be computationally predicted [30]. Examination of dopability via the corresponding defect diagram can offer useful insights for an approximation before experiments. Based on dopability, semiconductors can be categorized into four types: p-type dopable, n-type dopable, n- and p-type dopable, and neither n- nor p-type dopable. Take a p-type dopable material as an example (Figure 4a): in a material with relatively low formation energy of intrinsic acceptor defects and relatively high formation energy of intrinsic donor defects, extrinsic p-type doping is energetically favorable. For n-type doping, electrons introduced by the extrinsic dopants are compensated by intrinsic acceptors. Consequently, the native acceptor dopant concentration limits the extrinsic dopant concentration. By contrast, for p-type doping, the holes introduced by the extrinsic acceptor dopants are not significantly compensated due to the high formation energy of native

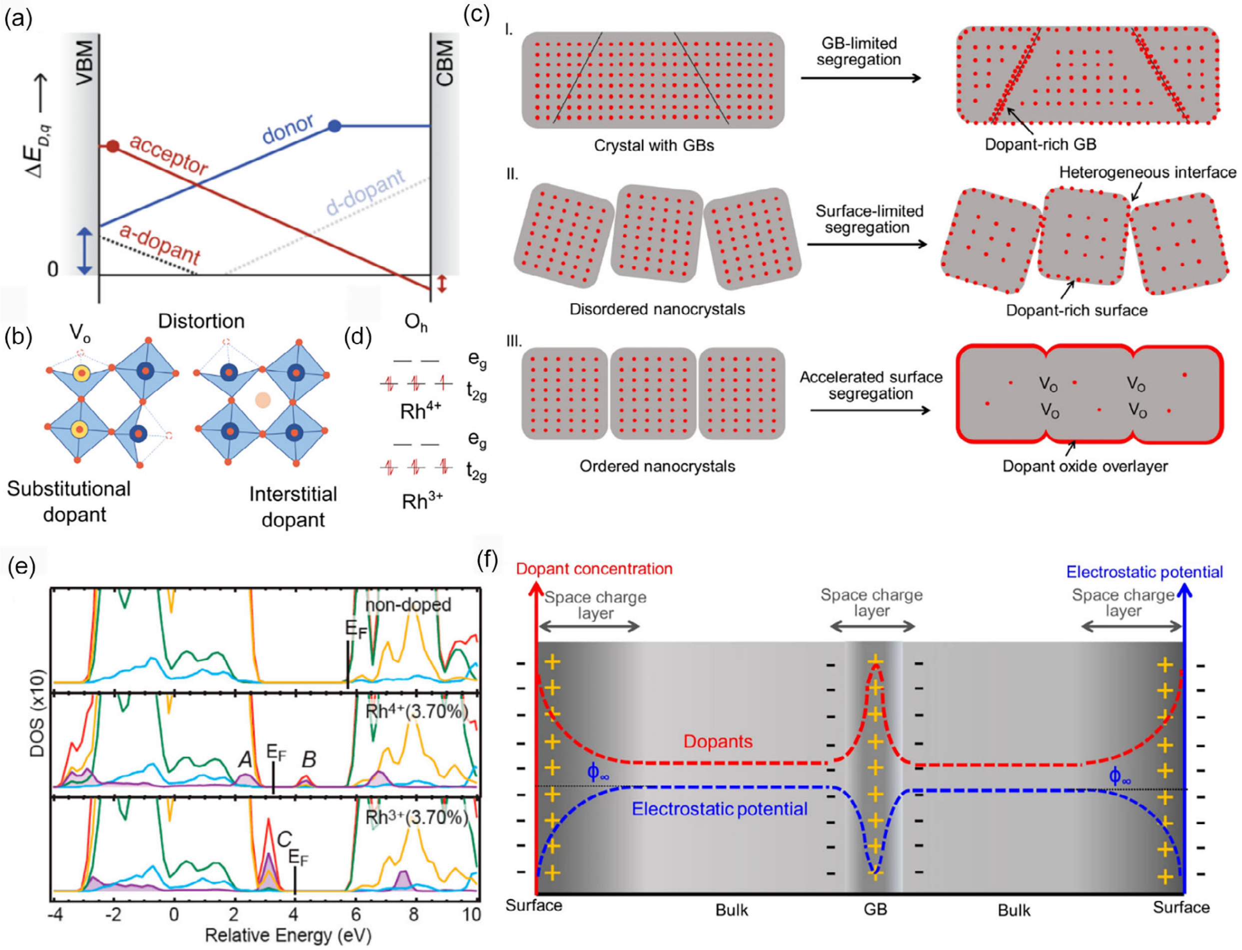

FIGURE 4 | Cationic doping-induced structure and electronic structure changes. (a) Defect diagram of a p-type dopable material. The formation energy of defect D with the charge state q ($\Delta E_{D,\,q}$) is plotted as a function of the Fermi energy. The blue arrow indicates p-type dopability window. The red arrow indicates n-type dopability window. The solid lines indicate intrinsic defects. The dashed lines indicate extrinsic doping. (b) Type of defects introduced by substitutional doping and interstitial doping. (c) Types of dopant segregation in ionic oxide crystals: (I) Crystal with numerous grain boundaries (GB): dopants tend to segregate at the surface and GBs. (II) Disordered nanocrystals: a small number of dopants tend to segregate on the surface due to the lack of driving force, even at high temperatures. (III) Ordered nanocrystals with highly aligned interfaces: a large number of dopants segregate on the outer surface because of interface sintering (GB elimination), creating numerous interfacial oxygen vacancies (V_O). (d) Crystal field splitting of 4d electrons in Rh^{3+} and Rh^{4+} in an octahedral (O_h) coordination environment. (e) Density of states obtained by first-principles calculations for nondoped, Rh^{4+} doped, and Rh^{3+} doped $SrTiO_3$.The Rh^{4+} donor and acceptor levels are marked with A and B, respectively. The Rh^{3+} donor level is marked with C. A, B, and C states are derived from the Rh 4d t_{2g} orbitals. The Rh PDOS peaks in the conduction band region, at a relative energy of 6.5 eV for the Rh^{4+} sample and 7.5 eV for the Rh^{3+} sample, are derived from Rh 4d e_g orbitals. The midgap level B is an unoccupied down-spin state. Note that this state is destabilized by the short-range Hartree–Fock exchange interaction due to the existence of an unpaired electron at the Rh^{4+} (d5) site. In contrast, the Rh^{3+} (d6) sample does not have an unpaired electron and thus no midgap state. (f) Distribution of dopants and electrostatic potential in ionic oxides based on the space charge theory in the case of donor doping. Figure 4a reprinted under the terms of the Creative Commons Attribution 4.0 International license [30]. Copyright (2025), The Authors, published by the American Physical Society. Figure 4b adapted with permission from Ref. [25], copyright (2022) Springer Nature Limited. Figure 4c,f reprinted under a Creative Commons Attribution 4.0 International license [31]. Copyright (2022), The Authors, published by Springer Nature Limited. Figure 4e reprinted with permission from Ref. [32], copyright (2012) American Chemical Society.

donors. However, bear in mind that dopability reflects the energetic ease rather than certainty, because the solubility, ionization energy of dopants, and the synthesis conditions, such as temperature and oxygen partial pressure, also affect the actual doping, as suggested by the thermodynamic analysis. For example, n-type TiO_2 under Ti-rich conditions is calculated to be n-type dopable [33], meaning n-type dopants are easier to incorporate than p-type dopants, but TiO_2 can be doped with both n-type dopants, such as Nb, and p-type dopants, such as Rh [17, 34, 35].

4 | Structure and Electronic Structure Modification Induced by Cationic Doping

Cationic doping induces structural and electronic changes in metal oxides. Isovalent substitution primarily introduces local structural distortion and changes in lattice parameters due to the size difference between foreign cations and host cations [36, 37]. Aliovalent substitution and interstitial doping perturb the structure and the electroneutrality conditions of metal oxides, introducing interstitial dopants, cation vacancies, and oxygen vacancies to compensate for the charge imbalance, and inducing lattice distortions (Figure 4b) [36, 38]. Additionally, driven by elastic strain energy and electrostatic interactions, it is common for cationic dopants to segregate to surfaces, grain boundaries, and dislocations, leading to the inhomogeneous distribution of dopants (Figure 4c) [31, 39]. For example, in Rh-doped $SrTiO_3$ synthesized through a solid-state method, Rh concentrates at the surface of $SrTiO_3$ and forms a core/shell structure, where the core is undoped, and the shell is Rh-doped [15].

These structural modifications perturb the electronic structure. Generally, defect levels can be categorized into shallow levels and deep levels based on their location. Shallow states lie close to the band edge, usually within k_BT of around 26 meV at room temperature, so charge carriers can be delocalized and excited into the bands and thus contribute to the conductivity. By contrast, deep levels lie in the middle of the bandgap, and charge carriers are generally localized at room temperature, which can be introduced by cations with large size and charge mismatch with host cations and are generally related to large distortions [25]. Deep states play a complex role in charge transport, which will be discussed in a later section.

The dopant's electronegativity and binding energy of valence electrons can be used as a descriptor to qualitatively predict dopant-level position as a first approximation [25, 40]. For example, in substitutional Rh^{3+}-doped $SrTiO_3$, the valence band maximum is composed of O 2p orbitals, and the conduction band minimum is composed of Ti 3d orbitals. Since Rh is more electronegative than Ti, the valence electrons on Rh 4d orbitals are bound more tightly to the nuclei of Rh than those on Ti 3d orbitals. Therefore, Rh 4d orbitals are located more deeply than the conduction band edge composed of Ti 3d but above the valence band maximum of O 2p, thus forming intragap states. Furthermore, due to crystal field splitting, Rh^{3+} that substitutes for Ti is octahedrally coordinated to six O^{2-}. Therefore, their d orbitals split into two sets: lower energy t_{2g} (d_{xy}, d_{yz}, and d_{xz}) and higher energy e_g (dz_2 and dx_2-y_2) (Figure 4d). For Rh^{3+}, the electronic configuration is t_{2g}^6 [41]. For Rh^{4+}, orbital splitting gets more complicated, likely through lattice interaction (Figure 4e) [32, 42]. To compensate for the charge imbalance induced by Rh^{3+}, V_o are formed concurrently. In the presence of oxygen vacancies, Ti 3d-3d orbital interactions can form deep defect states [43]. Additionally, the local lattice distortion induced by cationic doping can lead to potential fluctuations in the conduction and valence bands [13]. Besides these point defects, the segregation of cations at surface can lead to the formation of space charge regions driven by Fermi level equilibration (Figure 4f) [31]. Furthermore, the flat band potential and quasi-Fermi-level position at the surface of photocatalyst under the working condition could also be tuned by cationic doping [42]. All of these have a profound impact on light absorption, charge carrier transport, and surface reactivity in photocatalysis, which will be described in the next section.

Given their significant impact, detailed analysis of the structure and electronic structure is essential to establish structure-activity relationships and to apply fine control over photocatalytic performance. The dopant position and defect location can be studied by both experimental and computational methods. Experimentally, to confirm successful doping and analyze the location of defect levels, a set of characterization methods can be used for rigorous analysis of dopant position and resulting structures, including X-ray diffraction (XRD), neutron diffraction, pair distribution functions (PDF), scanning transmission electron microscopy (STEM), X-ray photoelectron spectroscopy (XPS), X-ray absorbance spectroscopy (XAS), ultraviolet photoelectron spectroscopy (UPS), inverse photoemission spectroscopy (IPES), UV–vis spectroscopy, and electron paramagnetic resonance (EPR) [44, 45]. Computationally, the dopant level position is indicated by charge transition levels in defect diagram, and detailed states available at each energy level are shown in density of states (DOS) plot [30].

5 | Impact of Cation Doping on Photocatalysis

After establishing a foundation of photocatalysis and doping, we review the key progress on how cationic doping affects the three sequential steps using several representative photocatalysts. Currently, the last step involving surface reactions is largely unexplored due to the challenges of experimentally and computationally studying the surface dynamics under working conditions. Therefore, our emphasis in this section is on the first two steps, namely, light absorption and charge transport. In particular, great progress has been made in understanding the complex influence of cationic doping on charge separation step, enabled by the development of characterization techniques for ultrafast charge carrier dynamics detection and solid-state analysis in recent years [45].

5.1 | Single Cationic Doping

5.1.1 | Cationic Dopant Level Lies in Band

When cationic dopant levels lie above the band edge, they do not directly contribute to light absorption or significantly alter it. Instead, they can affect photocatalytic activity by modulating the charge carrier separation process through hybridizing with intrinsic defect states or conduction bands. For example, Al doping dramatically increased the photocatalytic overall water splitting activity of $SrTiO_3$, and an AQE of 30% was achieved at 360 nm, much higher than the 4.3% for undoped $SrTiO_3$. By selectively loading the cocatalyst Rh/Cr_2O_3 and cobalt oxyhydroxide (CoOOH) for HER and OER, respectively, on Al-doped $SrTiO_3$, consecutive forward charge transfers without backward charge transfer are achieved, enabling an external quantum efficiency of 94%, which is maintained at least for 12.5 h [14]. UV–vis suggested the incorporation of Al did not improve the light absorption properties of $SrTiO_3$ or modify the bandgap energy (Figure 5a) [47]. However, time-resolved photoluminescence (TRPL) spectra showed an extended intrinsic charge carrier lifetime due to the elimination of Ti^{3+} nonradiative recombination centers (Figure 5b), corroborated with an enhanced surface voltage [48]. Further diffuse reflectance transient spectroscopy (DRTS) and photoinduced absorption spectroscopy (PIAS) studies confirmed that the extended bulk charge carrier lifetime and diffusion length allow electron extraction by water at the surface before charge carrier recombination, thereby improving photocatalytic overall water splitting (Figure 5c,d) [46]. Computational analysis provided an orbital-wise understanding. It revealed that Al prefers to substitute Ti adjacent to oxygen vacancies, forming $[V_o\text{-}Al_{Ti}]$ complexes, and the absence of d valence orbitals in Al is the key to eliminating the trap states formed by Ti 3d-Ti

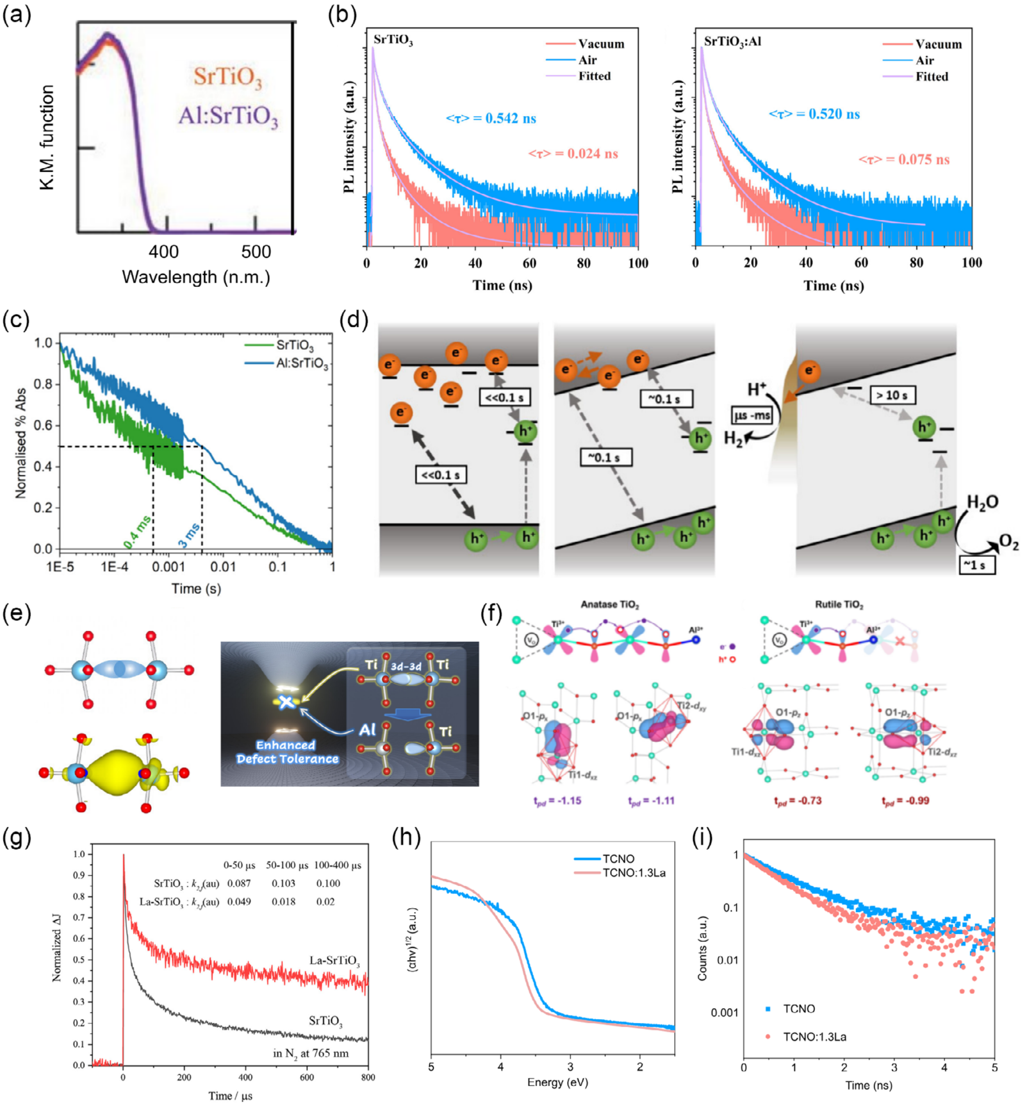

FIGURE 5 | (a) Tauc plots of undoped and Al-doped $SrTiO_3$ converted from UV–vis DRS spectra. (b) TRPL spectra of undoped (left) and Al-doped $SrTiO_3$ (right) in air and under vacuum. (c) DRTS kinetics of $SrTiO_3$ and Al: $SrTiO_3$ in H_2O probed at 500 nm, measured using 355 nm laser excitation at an intensity of 400 µJ cm^{-2} and a 0.8 Hz repetition rate. In addition to the increased signal amplitudes measured in DRTS and PIAS, lower DRTS decays in Al: $SrTiO_3$ highlight the ability of Al: $SrTiO_3$ to support larger charge carrier densities and lifetimes. (d) Charge separation and recombination in $SrTiO_3$ (left), Al: $SrTiO_3$ (middle), and Al: $SrTiO_3$/Rh(PD)/Cr_2O_3 (right) under steady-state irradiation for water splitting. Al^{3+} doping introduced the internal electric field indicated by sloped conduction and valence band, driving charge separation. Further selective deposition of $RhCrO_x$ in Al: $SrTiO_3$/Rh(PD)/Cr_2O_3 on the reduction facets facilitates electron extraction for proton reduction. The >10 s decay time represents the slow decay phase between deeply trapped holes and conduction band electrons, while the fast decay phase is represented by the ~1 s water oxidation reaction. (e) Schematic illustration of orbital interaction. On the right, the uneven charge density distribution in Ti 3d-Ti 3d interaction across the oxygen vacancy, which arises from the competition between orbital interaction, factoring charge distribution, and the Coulombic interaction, factoring electron localization. On the left, substitutional Al doping deactivates this interaction and eliminates the in-gap state. (f) Schematic illustration of electron hopping between Ti-t_{2g} and O- $p\pi$ orbitals in anatase TiO_2 (left) and rutile TiO_2 (right). Overlapping integral (t_{pd}) is more negative in anatase than in rutile TiO_2, thus confirming stronger p-d coupling between Ti-t_{2g} and O-$p\pi$ orbitals in anatase TiO_2 than in rutile TiO_2. (g) TAS of the undoped $SrTiO_3$ and La–$SrTiO_3$ in N_2 ambient at 765 nm. (h) Tauc plots and (i) TRPL spectra of La-doped $TBACa_2Nb_3O_{10}$. Figure 5a adapted with permission from Ref. [47], copyright (2023) Wiley-VCH GmbH. Figure 5b reprinted with permission from Ref. [48], copyright (2023) Wiley-VCH GmbH. Figure 5c,d reproduced under terms of the CC-BY license [46]. Copyright (2025), The Authors, published by the American Chemical Society. Figure 5e reproduced under terms of the CC-BY license [43]. Copyright (2025), The Authors, published by the American Chemical Society. Figure 5f reproduced with permission from Ref. [49] copyright (2025) American Physical Society. Figure 5g reprinted with permission from Ref. [50], copyright (2020) American Chemical Society. Figure 5h,i reproduced under terms of the CC-BY license [13]. Copyright (2025), The Authors, published by the American Chemical Society.

3d interactions across oxygen vacancies (Figure 5e) [43]. Furthermore, even when Al^{3+} and V_o are distantly separated in TiO_2, p-d coupling between Ti-t_{2g} and O-p (π) orbitals is still highly effective and facilitates electron hopping from V_o to distant holes, thereby leading to suppression of Ti^{3+} recombination centers (Figure 5f) [49].

In addition to interactions with intrinsic defect states, hybridization of dopant levels with the conduction bands has also been proposed to effectively enhance the photocatalytic HER activity. For example, La doping enhanced the photocatalytic HER of $SrTiO_3$ loaded with 1.0 wt% Pt from 379.2 to 550.4 μmol h^{-1} under UV–vis light irradiation. The hybridization of the conduction bands of $SrTiO_3$ and La 5d orbitals was found to secure the photoexcited electrons and extend the charge carrier lifetime (Figure 5g) [50]. However, the positive effects of La doping are not general for all hosts. Some contrasting results have been reported, where La doping significantly suppressed the photocatalytic HER activity. For example, in La-doped $TBACa_2Nb_3O_{10}$(TCNO), La doping reduced the photocatalytic HER activity to approximately one-tenth of that of the undoped layered perovskites [13]. It was found that La doping did not significantly alter the light absorbance of TCNO (Figure 5h) but shortened the lifetime of photogenerated charge carriers (Figure 5i). This decrease was attributed to the distorted NbO_6 octahedra induced by La doping, leading to strong local potential fluctuation and facilitating recombination. These results suggest the strong dependence of the doping effects on the host structure and the delicate interplay between the dopant and associated defects in photocatalysis.

5.1.2 | Cationic Dopant Level Lies Within Band Gap

Cationic dopant levels located within the bandgap can dramatically extend the light absorption properties of metal oxide photocatalysts even at low concentrations (Figure 6a). Such an effect originates from the optical transitions between defect states and bands, or between the defect states [25]. For example, in Rh-doped $SrTiO_3$, Rh substitutes at Ti sites and exists as Rh^{3+} and Rh^{4+}, opening up new transitions: the fully filled $\boldsymbol{t_{2g}}$states in Rh^{3+} allow $\boldsymbol{t_{2g}^6}$ - conduction band transitions, while the partially filled $\boldsymbol{t_{2g}}$ states in Rh^{4+} allow electronic transitions between bands and defect states [42, 51]. Furthermore, the midgap states introduced by Rh^{4+} also allow for the d–d transitions between $\boldsymbol{t_{2g}}$ of Rh^{3+} and $\boldsymbol{e_g}$ of Rh^{4+} [32, 51]. Additionally, the increase of oxygen vacancies also leads to the enhancement of absorption in the Infrared (IR) range due to optical transitions from the oxygen vacancy states to the conduction band. These new electronic transitions greatly extend the light absorption from the UV range to the IR range [17, 32].

However, not all photoexcited charge carriers contribute to the photocatalytic water splitting reaction, and the extension of light

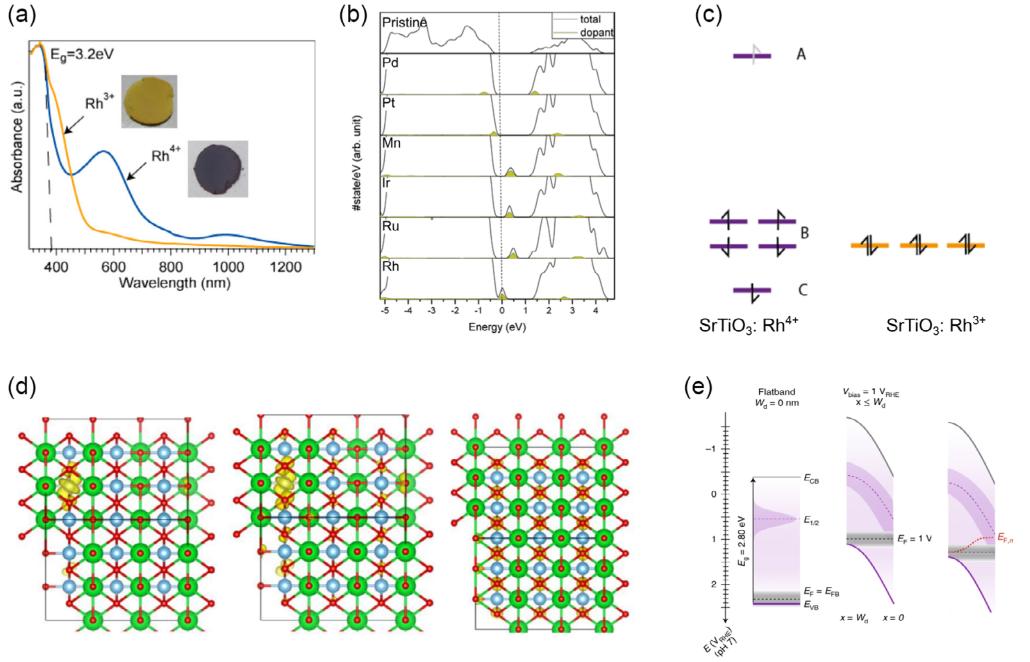

FIGURE 6 | (a) UV–vis-NIR absorption spectra of Rh^{3+}/Rh^{4+}-doped $SrTiO_3$. (b) Calculated density of states of undoped and different metal-doped $SrTiO_3$. Take Ru and Rh for comparison. A larger energy gap between the valence band (VB) and the Ru states indicates a strong charge-trapping nature. In addition, the higher Ru-states compared to Rh-states imply a weaker driving force for the oxidation reaction. (c) Splitting of the Rh 4d dopant states responsible for visible light harvesting in Rh^{4+} (left) and Rh^{3+} (right)-doped $SrTiO_3$. Three states exist in the band gap of Rh^{4+}-doped $SrTiO_3$: a vacant mid gap level above the Fermi level (A), an overlapping set of spin-up and spin-down states just beneath the Fermi level (B), and a single spin-down state (C). Rh^{3+}-doped $SrTiO_3$ only shows a single set of filled states just beneath the Fermi level within the band gap. (d) Iso-surfaces of the Rh 4d states situated above the valence band of $SrTiO_3$ (responsible for visible light absorption). On the right is an example of the lowest energy-filled Rh state observed in Rh: $SrTiO_3$. In the middle is an example of the vacant mid-gap state observed in Rh: $SrTiO_3$. On the right is an example of a typical O 2p valence band state in $SrTiO_3$, showing a high degree of delocalization. (e) Surface depletion model of Rh^{4+}-doped $SrTiO_3$ at flat band potential (left) and 1 V_{RHE} (middle). On the right, photovoltage builds up in Rh^{3+}/Rh^{4+} doped $SrTiO_3$ under illumination at positive device operation potentials. Conduction band (CB) electrons can accumulate due to the downward band bending. However, electron trapping processes likely induced by Rh^{4+} states prevent the accumulation of electrons in CB, indicated by a quasi-Fermi level pinned to the Rh^{4+} redox potential. Figure 6a reprinted with permission from Ref. [32], copyright (2012) American Chemical Society. Figure 6b adapted with permission from Ref. [54], copyright (2012) American Chemical Society. Figure 6c-e adapted with permission from Ref. [42], copyright (2021) Springer Nature Limited.

absorption does not guarantee an increase in photocatalytic activity [52, 53]. As we have described in the previous section, the electrochemical potential determines the reactivity of photoexcited charge carriers, and the overall photocatalytic activity is also influenced by charge separation and extraction efficiency. In fact, in the cases of Mn, Ru, and Ir-doped $SrTiO_3$, despite the extended light absorption, a dramatic decrease in photocatalytic HER activity has been observed [16]. Several factors have been identified for the loss of activity. First of all, thermodynamically speaking, photoexcited charge carriers located at defect levels might lack the necessary driving force to satisfy the thermodynamic requirements for water splitting. For example, the energy states introduced by Ru in $SrTiO_3$ are significantly above the valence band maximum, meaning the electrochemical potential of photogenerated holes located on the Ru mid-gap states is more negative than the water oxidation potential [54, 55]. Therefore, these photogenerated holes cannot transfer to water and become inactive for the reaction. More importantly, the isolated deep states formed by Ru promote charge recombination, reducing the concentrations of free charge carriers with sufficient driving force (Figure 6b) [54].

A special case involves Rh^{3+}, which has paired electrons and filled t_{2g} states under the octahedral coordination environment. Rh^{3+} t_{2g} states have been discovered as selective trapping sites for hole carriers, offering an alternative relaxation pathway of photoexcited charge carriers beyond band–band relaxation, aiding charge separation at the expense of some driving force, and ultimately improving catalytic activity [53]. Although Rh^{3+} levels are located hundreds of meV above the valence band maximum, they hybridize with the valence band, rather than forming isolated states, which allows for efficient charge transfer and reduces the probability of immobilization of charge carriers [42, 54].

Besides modulating the charge separation process within the bulk, cationic doping also disrupts the equilibrium of the density states indicated by the Fermi level position, tuning the band bending direction and magnitude of the photocatalyst under working conditions, which is a common driving force of charge carrier separation at the surface in photocatalysts with good crystallinity and few surface defects. In the case of Rh^{3+}-doped $SrTiO_3$, size exclusion chromatography (SEC) and transient absorption (TA) analysis revealed Rh doping switched $SrTiO_3$ from an n-type semiconductor to a p-type semiconductor, forming a depletion region within $SrTiO_3$ at the interface and dramatic downward band bending, which provided a strong driving force for charge separation and facilitated charge accumulation in conduction band [42]. Despite the beneficial role of Rh^{3+}, the coexistence of Rh^{4+} in $SrTiO_3$ limits its performance by introducing mid-gap states, which trap electrons and prevent the electron accumulation in the conduction band, thus leading to Fermi-level pinning below Rh^{4+} and deteriorating the photocatalytic HER activity (Figure 6c–e).

These results clearly indicate that the enhancement of light absorption is not the determinative step, and effective separation and extraction of photogenerated charge carriers are more influential.

5.2 | Codoping

To offset the liabilities of single-doping approach and further enhance the photocatalytic activity, codoping strategies have been widely explored by introducing complementary dopants that compensate and modulate defect states. Combinations in which one dopant lies within the bandgap and the other lies above the conduction band, such as Rh/La and Rh/Bi in $SrTiO_3$, and combinations in which both dopants lie above the conduction band, such as Al/La in $SrTiO_3$, have been explored in the literature.

When introducing a codopant state that lies above the conduction band in conjunction with dopant states that lie deeply within the bandgap, earlier research often broadly attributed the improved activity to charge compensation effect of codopants, which mitigates the trap defects intrinsically introduced by aliovalent doping due to charge imbalance. For example, La codoping of $SrTiO_3$ with Rh improved the photocatalytic HER activity, which was correlated with the suppression of the Rh^{4+} midgap states and the stabilization of Rh^{3+}.

Recent research has deepened the understanding of codopants' important roles in charge-transfer modulation within the bulk and at the interface. For example, in Rh and La co-doped $SrTiO_3$, La^{3+} could not only suppress Rh^{4+} but also stabilize Rh^{3+} even at very positive potentials (Figure 7a,b). The modified electronic structure leads to effective charge separation under the driving force of band bending in the depletion region at the interface while avoiding charge traps, thereby enhancing photocatalytic activity (Figure 7c,d) [42].

The identification of Bi as a more efficient codopant than La for Rh marks an important milestone in codoping strategies (Figure 7e) [56]. The exceptional AQE of 18.9% at 420 nm highlights the crucial role of Bi in suppressing oxygen vacancy formation, which commonly serves as a recombination center in La/Rh-doped $SrTiO_3$. Furthermore, surface-concentrated Bi/Rh synthesized via the solid-molten synthesis method enables a short migration distance of photogenerated charge carriers, delivering superior photocatalytic HER activity compared with their bulk-doped counterparts.

The understanding of codoping strategies has been further advanced by the recent demonstration of synergistic effects and functional separation of codopants in Rh/La codoped two-dimensional Dion-Jacobson-type layered perovskite $TBACa_2Nb_3O_{10}$ (Figure 7f-i) [13]. The function of Rh was clearly demonstrated as charge separation mediator, while the function of La extends beyond charge compensation to include structural modulation. Specifically, Rh^{3+} substitutes Nb^{5+} sites and introduces acceptor levels 0.9 eV above the valence band maximum, facilitating photocatalysis through trap-mediated selective hole capture. In contrast, La^{3+} serves as a charge compensator and structural stabilizer, enhancing Rh^{3+} incorporation and dispersion, suppressing oxygen vacancies, and distorting structures without directly contributing electronic states. Benefiting from the synergistic effect, Rh/La-codoped $TBACa_2Nb_3O_{10}$ nanosheets achieved a fivefold increase in photocatalytic HER with a high H_2 evolution rate of 69.0 μmol h^{-1} under full-arc irradiation and an AQE of 12.99% at 405 nm at the optimal Rh/La codoping level.

When introducing a codopant state that lies above the conduction band alongside a single dopant that lies above the conduction band, codoping has been found to reduce the segregation of dopants and host cations. For example, La doping increases the solubility and dispersion of Al. In La/Al codoped $SrTiO_3$, codoping La with Al at small concentrations (1% Al 0.6% La) helps

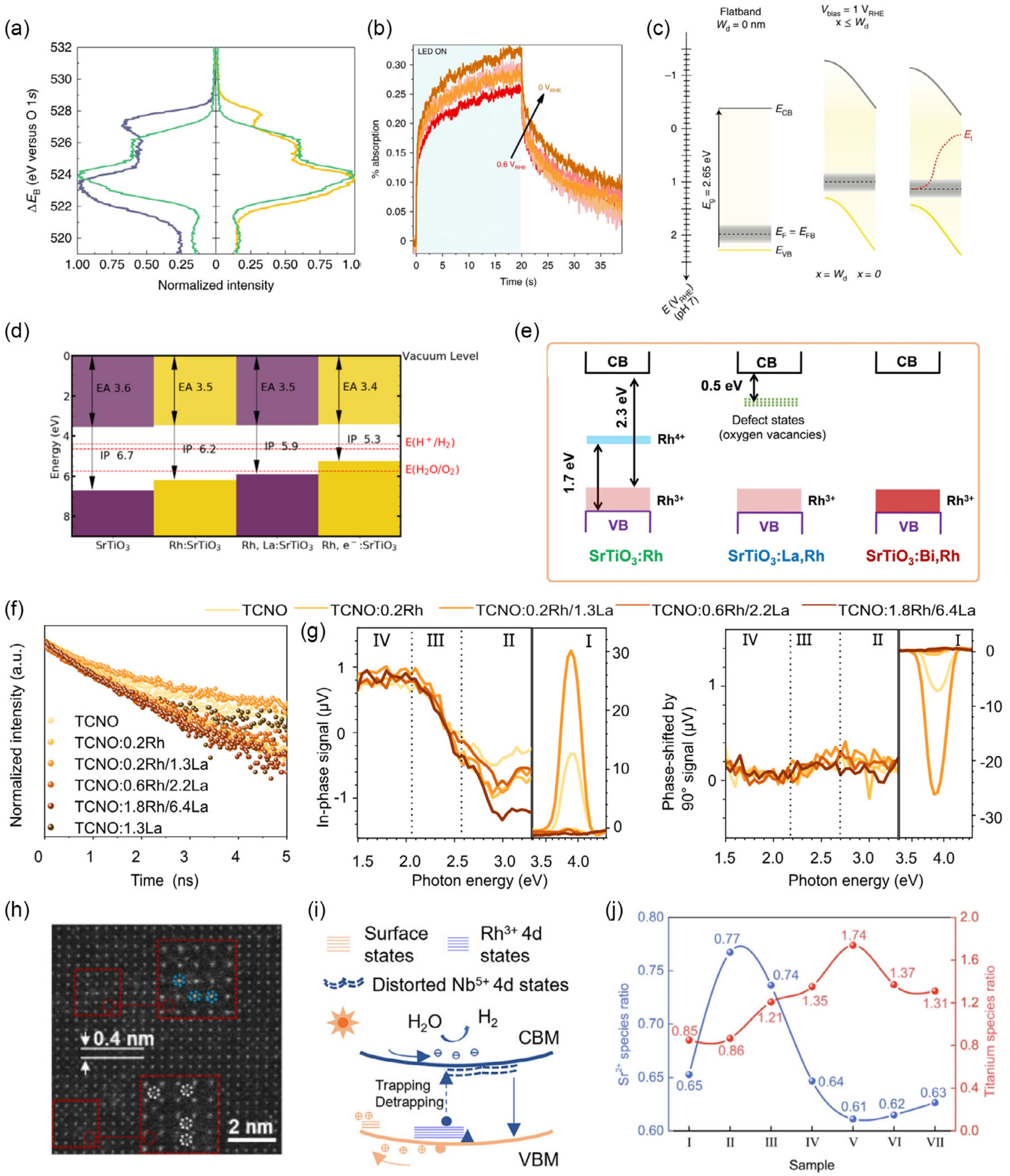

FIGURE 7 | (a) Valence band (VB) spectra of SrTiO$_3$ (green), Rh:SrTiO$_3$ (purple), and La, Rh:SrTiO$_3$ (yellow) on the ΔE_B scale for the comparison of the energy of the Rh dopant states. Rh doping introduces intragap states of SrTiO$_3$, leading to a broadening of the VB envelope and a narrowing of the effective bandgap. La codoping shifts the states to a higher energy, implying the reduction of Rh^{4+} by La. (b) Photoinduced absorption (PIA) kinetics in La, Rh:SrTiO$_3$ photocatalyst sheets at various applied potentials are broadly potential independent, indicating La-assisted stabilization of Rh^{3+}. (c) Surface depletion model in La, Rh: SrTiO$_3$ at flat band potential condition and 1 V_{RHE}. The substantial band bending in La, Rh: SrTiO$_3$ drives electron accumulation, which leads to an effective charge separation, as indicated by $E_{F,\ n}$ reaching toward the CB. (W_d indicates the width of the space charge layer). (d) Calculated band alignment of Rh: SrTiO$_3$, La, Rh: SrTiO$_3$, and Rh:SrTiO$_3$ in the presence of a compensating background charge (Rh:SrTiO$_3$ + e$^-$). EA stands for electron affinity, and IP stands for ionization potential. (e) Electronic-structure diagrams of SrTiO$_3$: Rh, SrTiO$_3$: La, Rh, and SrTiO$_3$: Bi, Rh. (f) TRPL spectra of undoped and Rh/La-doped TBACa$_2$Nb$_3$O$_{10}$. The longest lifetime was obtained for TCNO:0.2Rh/1.3La. (g) SPV spectra of undoped and Rh/La-doped TBACa$_2$Nb$_3$O$_{10}$. The most intense surface photovoltage was obtained for TCNO:0.2Rh/1.3La. (h) High-resolution HAADF–STEM image of TCNO:0.2Rh/1.3La. Rh substituted at B site (white circles) and La substituted at A site (blue circles). (i) Illustration of synergistic effects and proposed trap-mediated charge separation mechanism in Rh/La codoped TCNO. (j) Sr^{2+} and titanium species ratio in La/Al doped SrTiO$_3$ obtained from XPS spectra: (I) pure STO, (II) Al (1.0)-STO, (III) La, Al (0.2,1.0)-STO, (IV) La, Al (0.4,1.0)-STO, (V) La, Al (0.6,1.0)-STO, (VI) La, Al (0.8,1.0)-STO, (VII) La, Al (1.0,1.0)-STO. Figure 7a–d reprinted with permission from Ref. [42], copyright (2021) Springer Nature Limited. Figure 7e reprinted with permission from Ref. [56], copyright (2024) Wiley-VCH GmbH. Figure 7f i reproduced under terms of the CC-BY license [13]. Copyright (2025), The Authors, published by the American Chemical Society. Figure 7j reprinted with permission from Ref. [57], copyright (2021) American Chemical Society.

make Sr^{2+} re-enter the lattice, reduces surface segregation of Sr^{2+}, and promotes the conversion of Ti^{3+} to Ti^{4+}(Figure 7j), which improves the AQE from 42.07% for Al-doped $SrTiO_3$ to 78.34% for La/Al codoped $SrTiO_3$ at 365 nm [57].

Although the codoping strategy has shown great potential in the suppression of recombination centers introduced by single doping, the overall enhancement strongly depends on the interplay between codopants. For example, in Ni/Ta codoped $SrTiO_3$, despite Ta codoping increasing the lifetime of photogenerated electrons and enhancing the photocatalytic HER in the visible light region, the photocatalytic HER activity in the UV range dramatically decreased. Although Ta could compensate for the charge imbalance introduced by Ni^{2+}/Ni^{3+}, the number of defects that deep-trap electrons actually increased by Ni/Ta codoping [58].

6 | Summary and Outlook

Over the past decades, tremendous progress has been made in understanding how cationic doping modulates photocatalytic performance. The research focus has been shifting from dopant identification and concentration optimization to structure design and the exploration of mechanistic insight. It has become evident that the light absorption range alone does not guarantee improved activity. Instead, sufficient electrochemical potential, efficient separation, long lifetime, and fast extraction of photogenerated charge carriers play a decisive role in photocatalytic performance. With the development of transient spectroscopies and advanced solid-state characterization techniques, the multifaceted roles of cationic dopants have been elucidated with increasing clarity, particularly in the modulation of the charge carrier separation and recombination. These developments have deepened our insight into how cationic doping affects charge transport processes both in the bulk and at the solid–liquid interface. Moreover, codoping strategies have helped overcome some intrinsic limitations of single doping, revealing synergistic interactions and distinct functions of codopants. As these pieces of knowledge have been coming together, the design of photocatalysts has become more rational and focused, and the photocatalytic performance of these photocatalysts has reached new records one after another.

These achievements and findings open up new questions. The fundamental origins governing the defect role remain unresolved, particularly the correlation between electronic configuration, spin state, and charge carrier separation. Likewise, spin effects related to cationic doping in light absorption and surface reactions are largely unexplored, which can provide new avenues to tune the photocatalytic process [59]. Furthermore, the influence of cationic doping on surface reactions remains uncharted, mostly due to the difficulties of carrying out operando studies. However, it is foreseen that the development of time-resolved and operando spectroscopies will greatly contribute to the field. Moreover, the dynamic shift of thermodynamic driving forces might enable the research of previously ignored cations.

Acknowledgments

M. D. acknowledges financial support from the EPSRC Doctoral Training Partnership (Grant ref EP/T517811/1).

Funding

This work was funded by the Engineering and Physical Sciences Research Council (EP/T517811/1).

Conflicts of Interest

The authors declare no conflicts of interest.

References

1. T. Hisatomi, T. Yamada, H. Nishiyama, T. Takata, and K. Domen, "Materials and Systems for Large-Scale Photocatalytic Water Splitting," *Nature Reviews Materials* 10 (2025): 769–782.

2. Q. Wang and K. Domen, "Particulate Photocatalysts for Light-Driven Water Splitting: Mechanisms, Challenges, and Design Strategies," *Chemical Reviews* 120 (2020): 919–985.

3. Z. Wang, C. Li, and K. Domen, "Recent Developments in Heterogeneous Photocatalysts for Solar-Driven Overall Water Splitting," *Chemical Society Reviews* 48 (2019): 2109–2125.

4. S. Nishioka, F. E. Osterloh, X. Wang, T. E. Mallouk, and K. Maeda, "Photocatalytic Water Splitting," *Nature Reviews Methods Primers* 3 (2023): 42.

5. T. Hisatomi and K. Domen, "Reaction Systems for Solar Hydrogen Production via Water Splitting with Particulate Semiconductor Photocatalysts," *Nature Catalysis* 2 (2019): 387–399.

6. H. Gerischer, "Electrochemical Behavior of Semiconductors under Illumination," *Journal of the Electrochemical Society* 113 (1966): 1174.

7. A. Fujishima and K. Honda, *"Electrochemical Photolysis of Water at a Semiconductor Electrode" Nature* 238 (1972): 37–38.

8. R. Asahi, T. Morikawa, H. Irie, T. Ohwaki,"Nitrogen-Doped Titanium Dioxide as Visible-Light-Sensitive Photocatalyst: Designs, Developments, and Prospects," *Chemical reviews* 114 (2014): 9824–9852.

9. H. Li, Y. Zhou, W. Tu, J. Ye, and Z. Zou, "State-of-the-Art Progress in Diverse Heterostructured Photocatalysts toward Promoting Photocatalytic Performance," *Advanced Functional Materials* 25 (2015): 998–1013.

10. J. Ran, J. Zhang, J. Yu, M. Jaroniec, and S. Z. Qiao, "Earth-Abundant Cocatalysts for Semiconductor-Based Photocatalytic Water Splitting," *Chemical Society Reviews* 43 (2014): 7787–7812.

11. N. Wang, L. Cheng, Y. Liao, and Q. Xiang, "Effect of Functional Group Modifications on the Photocatalytic Performance of g-C_3N_4," *Small* 19 (2023): 2300109.

12. Y. Li, Z. Wang, Y. Wang, et al., "Local Magnetic Spin Mismatch Promoting Photocatalytic Overall Water Splitting with Exceptional Solar-to-Hydrogen Efficiency," *Energy & Environmental Science* 15 (2022): 265–277.

13. M. Duan, S. Guo, W. Niu, et al., "Synergistic Rh/La Codoping Enables Trap-Mediated Charge Separation in Layered Perovskite Photocatalysts," *Journal of the American Chemical Society* 147 (2025): 38599–38608.

14. T. Takata, J. Jiang, Y. Sakata, et al., "Photocatalytic Water Splitting with a Quantum Efficiency of Almost Unity," *Nature* 581 (2020): 411–414.

15. Q. Wang, T. Hisatomi, S. S. K. Ma, Y. Li, and K. Domen, "Core/Shell Structured La-and Rh-Codoped $SrTiO_3$ as a Hydrogen Evolution Photocatalyst in Z-Scheme Overall Water Splitting under Visible Light Irradiation," *Chemistry of Materials* 26 (2014): 4144–4150.

16. R. Konta, T. Ishii, H. Kato, and A. Kudo, "Photocatalytic Activities of Noble Metal Ion Doped $SrTiO_3$ under Visible Light Irradiation," *The Journal of Physical Chemistry B* 108 (2004): 8992–8995.

17. R. Niishiro, R. Konta, H. Kato, W.-J. Chun, K. Asakura, and A. Kudo, "Photocatalytic O_2 Evolution of Rhodium and Antimony-Codoped

Rutile-Type TiO_2 under Visible Light Irradiation," *The Journal of Physical Chemistry C* 111 (2007): 17420–17426.

18. S. Chen, T. Takata, and K. Domen, "Particulate Photocatalysts for Overall Water Splitting," *Nature Reviews Materials* 2 (2017): 17050.

19. A. J. Kaufman, A. C. Nielander, G. J. Meyer, S. Maldonado, S. Ardo, and S. W. Boettcher, "Absolute Band-Edge Energies Are over-Emphasized in the Design of Photoelectrochemical Materials," *Nature Catalysis* 7 (2024): 615–623.

20. A. Sert, A. Mathur, and S. Linic, "Reactive Chemical Environments Control Charge Carrier Selectivity and Photovoltage at Nanoparticle Electrocatalyst/Semiconductor Junctions in Solar Water Splitting," *Journal of the American Chemical Society* 147 (2025): 30829–30841.

21. Z. Pan, R. Yanagi, Q. Wang, et al., "Mutually-Dependent Kinetics and Energetics of Photocatalyst/Co-Catalyst/Two-Redox Liquid Junctions," *Energy & Environmental Science* 13 (2020): 162–173.

22. J. Wang, W. Liao, Y. Tan, et al., "Transfer Dynamics of Photo-Generated Carriers in Catalysis," *Chemical Society Reviews* 54 (2025): 6553–6596.

23. Y. Li, H. Zhou, S. Cai, et al., "Electrolyte-Assisted Polarization Leading to Enhanced Charge Separation and Solar-to-Hydrogen Conversion Efficiency of Seawater Splitting," *Nature Catalysis* 7 (2024): 77–88.

24. K. Maeda, "Photocatalytic Water Splitting Using Semiconductor Particles: History and Recent Developments," *Journal of Photochemistry and Photobiology C: Photochemistry Reviews* 12 (2011): 237–268.

25. E. Pastor, M. Sachs, S. Selim, J. R. Durrant, A. A. Bakulin, and A. Walsh, "Electronic Defects in Metal Oxide Photocatalysts," *Nature Reviews. Materials* 7 (2022): 503–521.

26. H. L. Tuller and S. R. Bishop, "Point Defects in Oxides: Tailoring Materials through Defect Engineering," *Annual Review of Materials Research* 41 (2011): 369–398.

27. U. Balachandran and N. G. Eror, "Solubility of Lanthanum in Strontium Titanate," *Journal of the American Ceramic Society* 64 (1981): c–75-c-76.

28. F. Fujishiro, T. Arakawa, and T. Hashimoto, "Substitution Site and Photoluminescence Spectra of Eu^{3+}-Substituted $SrTiO_3$ Prepared by Pechini Method," *Materials Letters* 65 (2011): 1819–1821.

29. E. Ertekin, V. Srinivasan, J. Ravichandran, et al., "Interplay between Intrinsic Defects, Doping, and Free Carrier Concentration in $SrTiO_3$ Thin Films," *Physical Review B* 85 (2012): 195460.

30. P. Gorai, "Beginner's Guide to Interpreting Defect and Defect Level Diagrams," *PRX Energy* 4 (2025): 032001.

31. Z. Zhang, T. Tsuchimochi, T. Ina, et al., "Binary Dopant Segregation Enables Hematite-Based Heterostructures for Highly Efficient Solar H_2O_2 Synthesis," *Nature Communications* 13 (2022): 1499.

32. S. Kawasaki, K. Akagi, K. Nakatsuji, et al., "Elucidation of Rh-Induced in-Gap States of Rh: $SrTiO_3$ Visible-Light-Driven Photocatalyst by Soft X-Ray Spectroscopy and First-Principles Calculations," *The Journal of Physical Chemistry C* 116 (2012): 24445–24448.

33. A. Boonchun, P. Reunchan, and N. Umezawa, "Energetics of Native Defects in Anatase TiO_2: A Hybrid Density Functional Study," *Physical Chemistry Chemical Physics* 18 (2016): 30040–30046.

34. J. Huang, G. Li, Z. Zhou, et al., "Efficient Photocatalytic Hydrogen Production over Rh and Nb Codoped TiO_2 Nanorods," *Chemical Engineering Journal* 337 (2018): 282–289.

35. T. Shiraiwa, T. Yamasaki, K. Kushimoto, J. Kano, and T. Omata, "Enhanced Proton Transport in Nb-Doped Rutile TiO_2: A Highly Useful Class of Proton-Conducting Mixed Ionic Electronic Conductors," *Journal of the American Chemical Society* 147 (2025): 30757–30767.

36. V. B. Tinti, A. Kabir, D. Z. de Florio, and V. Esposito," The Role of Dopant on the Defect Chemistry of Metal Oxides," in *Metal Oxide Defects* Eds. V. Kumar, S. Som, V. Sharma, H. C. Swart (Elsevier, 2023), 313–353.

37. B. Koo, J. Seo, J. K. Kim, and W. Jung, "Isovalent Doping: A New Strategy to Suppress Surface Sr Segregation of the Perovskite O_2-Electrode for Solid Oxide Fuel Cells," *Journal of Materials Chemistry A* 8 (2020): 13763–13769.

38. A. Zunger, *Practical Doping Principles*, (National Renewable Energy Lab. (NREL) 2003).

39. W. Lee, J. W. Han, Y. Chen, Z. Cai, and B. Yildiz, "Cation Size Mismatch and Charge Interactions Drive Dopant Segregation at the Surfaces of Manganite Perovskites," *Journal of the American Chemical Society* 135 (2013): 7909–7925.

40. A. Walsh and K. T. Butler, "Prediction of Electron Energies in Metal Oxides," *Accounts of Chemical Research* 47 (2014): 364–372.

41. M. Kučera, J. Kuneš, and R. Gerber, "Magneto-Optical Effects of Rh^{3+} and Rh^{4+} Doped Yttrium Iron Garnet," *Journal of Applied Physics* 85 (1999): 5986–5988.

42. B. Moss, Q. Wang, K. T. Butler, et al., "Linking In Situ Charge Accumulation to Electronic Structure in Doped $SrTiO_3$ Reveals Design Principles for Hydrogen-Evolving Photocatalysts," *Nature Materials* 20 (2021): 511–517.

43. K. Ogawa, S. R. Kavanagh, F. Oba, and A. Walsh, "Defect Tolerance via External Passivation in the Photocatalyst $SrTiO_3$: Al," *Journal of the American Chemical Society* 147 (2025): 23180–23191.

44. E. W. McFarland and H. Metiu, "Catalysis by Doped Oxides," *Chemical Reviews* 113 (2013): 4391–4427.

45. C. Kranz and M. Wächtler, "Characterizing Photocatalysts for Water Splitting: From Atoms to Bulk and From Slow to Ultrafast Processes," *Chemical Society Reviews* 50 (2021): 1407–1437.

46. A. A. Wilson, B. Moss, A. A. Riaz, et al., "Long-Lived Hole Accumulation in Al: $SrTiO_3$/Rh–Cr Photocatalyst Systems under Continuous Irradiation and Its Correlation with Overall Water Splitting Efficiency," *Journal of the American Chemical Society* 147 (2025): 34438–34448.

47. D. H. Murthy, V. Nandal, A. Furube, et al., "Origin of Enhanced Overall Water Splitting Efficiency in Aluminum-Doped $SrTiO_3$ Photocatalyst," *Advanced Energy Materials* 13 (2023): 2302064.

48. R. Li, T. Takata, B. Zhang, et al., "Criteria for Efficient Photocatalytic Water Splitting Revealed by Studying Carrier Dynamics in a Model Al-Doped $SrTiO_3$ Photocatalyst," *Angewandte Chemie International Edition* 62 (2023): e202313537.

49. K. Zhang, L.-C. Yin, and G. Liu, "Suppression of Ti^{3+} Recombination Centers in Ti-Based Metal Oxide Photocatalysts by Al Doping," *Physical Review B* 111 (2025): 075127.

50. F. Ichihara, F. Sieland, H. Pang, et al., "Photogenerated Charge Carriers Dynamics on La-and/or Cr-Doped $SrTiO_3$ Nanoparticles Studied by Transient Absorption Spectroscopy," *The Journal of Physical Chemistry C* 124 (2020): 1292–1302.

51. E. N. K. Glover, S. G. Ellington, G. Sankar, and R. G. Palgrave, "The Nature and Effects of Rhodium and Antimony Dopants on the Electronic Structure of TiO_2: Towards Design of Z-Scheme Photocatalysts," *Journal of Materials Chemistry A* 4 (2016): 6946–6954.

52. T. Takata and K. Domen, "Defect Engineering of Photocatalysts by Doping of Aliovalent Metal Cations for Efficient Water Splitting," *The Journal of Physical Chemistry C* 113 (2009): 19386–19388.

53. X. Ma, X. Cui, Z. Zhao, M. A. Melo, E. J. Roberts, and F. E. Osterloh, "Use of Surface Photovoltage Spectroscopy to Probe Energy Levels and Charge Carrier Dynamics in Transition Metal (Ni, Cu, Fe, Mn, Rh) Doped $SrTiO_3$ Photocatalysts for H_2 Evolution From Water," *Journal of Materials Chemistry A* 6 (2018): 5774–5781.

54. H.-C. Chen, C.-W. Huang, J. C. S. Wu, and S.-T. Lin, "Theoretical Investigation of the Metal-Doped $SrTiO_3$ Photocatalysts for Water Splitting," *The Journal of Physical Chemistry C* 116 (2012): 7897–7903.

55. D. H. Murthy, H. Matsuzaki, Q. Wang, et al., "Revealing the Role of the Rh Valence State, La Doping Level and Ru Cocatalyst in Determining the H_2 Evolution Efficiency in Doped $SrTiO_3$ Photocatalysts," *Sustainable Energy Fuels* 3 (2019): 208–218.

56. Z. Pan, J. J. M. Vequizo, H. Yoshida, et al., "Simultaneous Structural and Electronic Engineering on Bi- and Rh-Co-Doped $SrTiO_3$ for Promoting Photocatalytic Water Splitting," *Angewandte Chemie International Edition* 64 (2025): e202414628.

57. Y. Qin, F. Fang, Z. Xie, et al., "La, Al-Codoped $SrTiO_3$ as a Photocatalyst in Overall Water Splitting: Significant Surface Engineering Effects on Defect Engineering," *ACS Catalysis* 11 (2021): 11429–11439.

58. A. Yamakata, M. Kawaguchi, R. Murachi, M. Okawa, and I. Kamiya, "Dynamics of Photogenerated Charge Carriers on Ni- and Ta-Doped SrTiO3 Photocatalysts Studied by Time-Resolved Absorption and Emission Spectroscopy," *The Journal of Physical Chemistry C* 120 (2016): 7997–8004.

59. Z. Wang, Y. Li, C. Wu, and S. C. E. Tsang, "Electric-/Magnetic-Field-Assisted Photocatalysis: Mechanisms and Design Strategies," *Joule* 6 (2022): 1798–1825.

Biographies

Mengqi Duan received her B.Eng. at Wuhan University of Technology in China in 2019 and M.S. at Cornell University under the supervision of Prof. Emmanuel P. Giannelis in 2021. She joined Prof. Shik Chi Edman Tsang's group at the University of Oxford in 2020 and currently is a Ph.D. candidate. Her current research focuses on catalyst design for photo and electrocatalytic water splitting.

Yiyang (Bruce) Li received his B.S. from Fudan University, China, in 2017, and his Ph.D. from the University of Oxford in 2022 under the supervision of the late Prof. Shik Chi Edman Tsang. He is currently a senior postdoctoral research associate in the Tsang Group. His research focuses on the synthesis, characterization, and performance evaluation of novel solid-state semiconductor materials, with an emphasis on both fundamental studies and practical applications in photocatalytic overall water splitting for renewable hydrogen production.

Shik Chi Edman Tsang (1962-2025) was a Professor of Inorganic Chemistry and Head of the Wolfson Catalysis Laboratory at the University of Oxford, UK. He also served as the catalysis theme coordinator in the department. His main research interests focused on nanomaterials and heterogeneous catalysis in the context of energy and the environment, including the development of catalytic, photocatalytic and electrocatalytic technologies for green chemistry, fine chemicals, cleaner combustion, energy storage, and production processes. He had particular expertise in the design and architecture of nanocatalysts, as well as in situ diffraction and spectroscopic characterization, which contributed to a deeper understanding of catalytic surfaces and interfaces.